Title: An anisotropic friction model in non-bonded flexible risers

Authors: Tianjiao Dai, Svein Sævik, Naiquan Ye

Abstract
The present paper addresses small scale friction tests and an anisotropic friction model to predict friction for the interface between the anti-wear tape and tensile armors in non-bonded flexible risers. Small scale friction tests were carried out to study the static and dynamic friction behavior, measuring the transition distance between static and dynamic friction and the associated friction coefficients under variable contact pressure. In addition, the anti-wear tape shear modulus was measured to validate the analytical solution of shear interaction stick stiffness, K_0, applied in previously proposed friction models. As grooves in the anti-wear tape surface were observed in the full scale test pipe, an anisotropic friction model was formulated and implemented into a computer code. Since the slip behavior will be influenced by the friction scaling factors, the K_0 and the sliding direction, numerical studies were carried out to investigated their effects on the friction forces and the axial stress ranges at the outermost fiber position. This was followed by a sensitivity study with respect to the effect of applying 1D (loxodromic) and 2D (geodesic) friction models on the axial stress range at the same position. At last, the effect of applying measured transition behavior in the static friction model was investigated.

1. Introduction

As flexible riser applications are moving into deeper water, challenges occur with respect to fatigue as a result of high mean and alternating stresses. A major component of the alternating stress is related to friction due to the relative motion between the helix elements and their supporting layers. The friction stress can be obtained from analytical solution or finite element analysis. For the finite element analysis, friction models can be applied as part of the shear interaction model, see Dai et al. [1]. However, there is uncertainty regarding how to consider groove geometry effects on longitudinal and transverse friction forces by applying the friction models. This may influence the fatigue life of flexible risers. It is hence of interest to develop an anisotropic friction model to correctly predict friction stress under such conditions.

Several authors have proposed methods to calculate the friction stress. Sødahl [4] and Sævik [5] only considered the longitudinal friction stress. Sævik [6] further proposed a 2D isotropic friction model and a similar model was applied by Sævik and Li [3] to study the tensile armor slip behavior. However, creep may occur forming grooves along the helix path if the flexible riser structure is operated under high pressure and temperature conditions or due to the manufacture procedures. Such grooves were observed in the test pipe [2], potentially causing different friction coefficients and K_0 in the axial and transverse directions. The methods mentioned above could not consider the anisotropic characteristics due to the anti-wear tape's creep deformation and the 2D friction model in [6] could not maintain constant K_0 under dynamic contact pressure. Therefore, an isotropic friction model is formulated for considering the groove geometry as well as investigating loxodromic and geodesic paths effects on the axial stress range.

Several authors have dealt with the anisotropic friction phenomena formulating the constitutive relationship of anisotropic friction with an analogy to the elastoplastic theory [7, 8, 9, 10]. Michalowski and Mroz [7] described the sliding rules of contact friction with reference to the rigid and elastoplastic material by applying plasticity theory. The sliding rules of rigid or elastoplastic material can be derived by the associated velocity rules using the friction limit condition, or the non-associated sliding potential function formulated by modeling the wedge asperities. Mroz [10] extended the analysis of Michalowski and Mroz [7] and described the limit friction condition and sliding potential function for a class of anisotropic friction models. Zmitrowicz [11, 12] defined the Coulomb friction tensor and formulated the friction force distributed on the interaction surfaces both characterized by the isotropic and anisotropic roughnesses. However, the stiffness matrix contributed by friction force was not formulated. Hashiguchi and Ozaki [13, 14, 15] further proposed an anisotropic friction model based on the unconventional plasticity theory. This friction model comprehensively described the smooth transition from static to dynamic friction with associated stiffness matrix. However, the static friction was found to have small effect on the friction moment and wire axial force at the outermost fiber position in a flexible riser [1]. Therefore, the present 2D friction model is based on the Coulomb friction concept without considering the static friction. A comprehensive isotropic Coulomb friction model including the yield function, non-associated sliding flow rule function and stiffness matrix was summarized in Belytschko et al.'s work [16]. The present anisotropic friction model is based on the ellipse yield function proposed by Mroz [7] and non-associated sliding flow rule. The terms related to tangential friction in the sliding potential flow rule are associated to the ellipse yield function. This is because a symmetric stiffness matrix is needed in the tangential plane to comply with the symmetric solver available in this case. The coupling terms related to the contact force versus tangential fraction were, therefore, omitted to avoid unphysical behavior during equilibrium iterations as noted in [16]. The proposed friction model also maintains constant shear interaction stick stiffness and allows for dynamic contact pressure which were not considered in [7, 13, 14, 15, 16].

Some measurements from small scale testing may be as accurate as those from full scale testing. By Dai et al. [1], the friction coefficients under variable contact pressure were determined by validating different friction models based on full scale test data reported by Skallerud [2]. For the static friction model, a transition distance equal to 2.0 was assumed, acting to describe the relation between static and dynamic slip distances. In addition, the shear interaction stick stiffness parameter, K_0, was applied in the friction models. The K_0 was proposed by Sævik and Li [3], which considered both the plane surfaces remain plane assumption and

the shear deformation of plastic layers. Good correlation was obtained by tuning the stick stiffness model with respect to the global bending moment versus the curvature data from full scale testing. Therefore, it is of interest to verify if these parameters can be obtained by small scale testing using the material from the full scale test pipe. If this can be done with sufficient accuracy, this will give benefit to the industry by reducing the need for full scale testing.

The objectives of the present work are hence summarized as follows:

1. Carry out small scale fiction tests to measure:
   1.1. the static and dynamic friction coefficient under variable contact pressure
   1.2. the shear modulus of the anti-wear tape
   1.3. the transition distance ratio in the static friction model.
2. Formulate the anisotropic friction model on the basis of constant shear interaction stick stiffness K_0 as well as dynamic contact pressure and implement the proposed anisotropic friction model into a computer code.
3. Investigate the friction scaling factor and K_0 effects on the axial stress range at the outermost fiber position and the associated transverse friction force for the anisotropic model.
4. Perform a sensitivity study with respect to the loxodromic and geodesic paths for investigating their effects on the axial stress range at the outermost fiber position and friction moment using the same model.
5. Carry out a sensitivity study to investigate the measured transition distance ratio effect on friction moment.

2. Experimental method

2.1. Motivations

Full scale testing was carried out by MARINTEK (SINTEF OCEAN, today) in 1991-1992 to investigate structural damping properties of dynamic flexible pipes [2]. The global bending moment versus curvature relationship was measured under variable internal pressure. The results were used to verify different friction models in [1]. For the static friction model, a transition distance equal to 2.0 was assumed, acting to describe the relation between static and dynamic slip distances. The test also served to determine the dynamic friction coefficients between the anti-wear tape and tensile wire under variable contact pressure by comparing the numerical results and full scale experimental data. An increasing friction coefficient was noted by decreasing contact pressure. In addition, the shear interaction stick stiffness parameter, K_0, was applied in the friction models. Good correlation was obtained with respect to the global bending moment versus the curvature data for an assumed value of K_0. Therefore, small scale testing was carried out for measuring the transition distance ratio, the anti-wear tape's shear modulus and friction coefficients under variable contact pressure, thus pointing the way forward with respect to obtaining these values for future applications.

2.2. Test setup

A sketch of the test setup is shown in Figure 1. This included motion control machine, load cell, weight, specimen (anti-wear tapes and tensile wire) and displacement sensor. Two anti-wire tapes were fixed on the rigid frame. The tensile wire was attached to the motion control machine which provided a cyclic relative displacement between the tapes and tensile wire. The load cell was used to record the friction force and the displacement sensor was applied to measure the precise displacement at the tensile wire left end. The contact load was controlled by the plates weight through the vertical cylinder. The contact part is zoomed

in Figure 1.

Validation tests were carried out for each component in the setup. It was discovered that the alignment between the tensile wire and tapes influenced the recorded friction behavior. As a hinge was required between the tensile wire and the load cell for reducing the potential bending moments in the load cell, the hinge induced rotation needed to be eliminated. Secondly, the displacement sensor frame was connected to a rigid frame and the sensor tip was attached to the tensile wire left end to accurately measure the tape's shear deformation. Further in order to accurately measure the shear modulus in the stick domain, it is very important to obtain full contact to ensure that the shear stress is fully activated over the full contact surface. However, full contact could not be achieved by straightening a curved tensile wire. Therefore, a standard steel bar was separately manufactured to measure the shear modulus. In addition, the tape was squeezed to have a flat surface with less irregularities. In order to remove start-up effects, the test specimen was further exposed to 2 hours of cyclic motion before data recording.

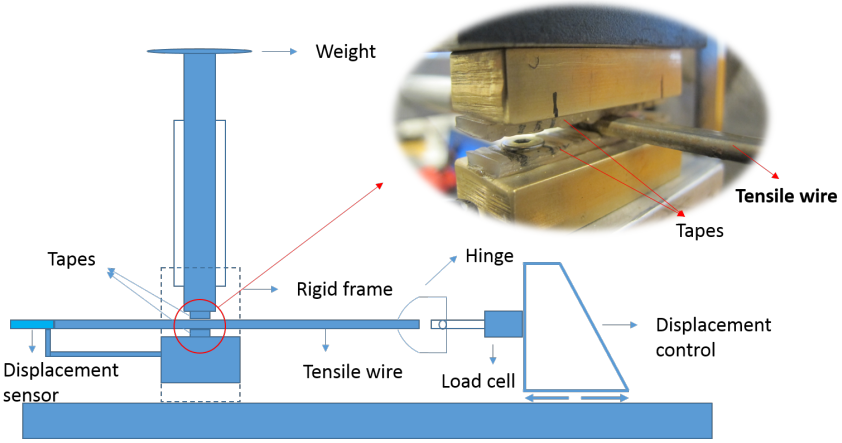

Figure 1: Small scale friction testing setup

2.3. Tests description

The test samples (tensile wire and anti-wear tape) were cut from the flexible pipe used in the full scale test mentioned in Section 2.1. Both the inner and outer surfaces of tape were used, see Figure 2. The groove geometry was observed on the inner surface, see Figure 2c. The typical velocity of tensile wires in flexible risers from wave loads is in the range 1-5 $[mm/s]$ with an associated frequency range of 0.01-0.2 $[Hz]$. A relative displacement amplitude 2 $[mm]$ and frequency in the range 0.01-0.2 $[Hz]$ were therefore applied in the tests. Three tests were carried out and the corresponding results and conclusions are presented in the Section 4.

3. Friction algorithm formulations

3.1. Introduction of anisotropic contact surface : anti-wear tape

Flexible risers are usually exposed to harsh environmental loads. In ultra deep waters, this combines with large tension and external pressure resulting in large contact pressure and cyclic bending loads. In order to avoid direct metallic contact and wear, the tensile layers are usually separated by a plastic anti-wear tape. This tape is subjected to significant contact pressure and long accumulative sliding distance. For example, the accumulative sliding distance for a 20 year design could be in the order of 50 km [17]. The anti-wear layers are typically made from polymeric tapes (e.g. PA6, PA11) with a thickness of 1 - 3 mm.

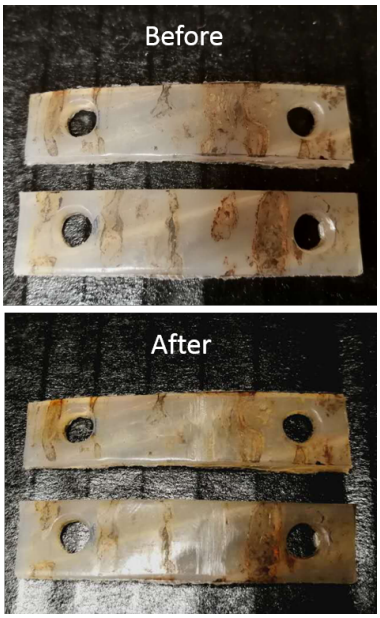

(a) Test No.1: outer surface of in-service tape

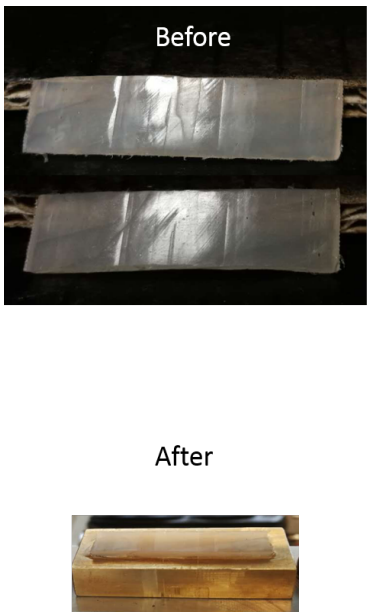

(b) Test No.2: outer surface of clean tape

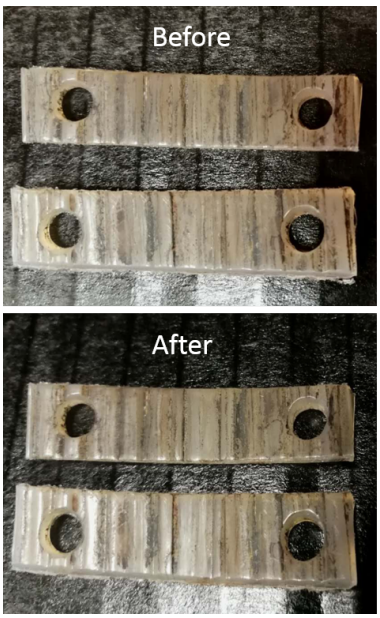

(c) Test No.3: inner surface (groove surface) of in-service tape

Figure 2: Three tests were carried out in the small scale testing. The anti-wire tape was cut from the same test pipe in the full scale testing. The anti-wire tape was used in the small scale testing for measuring the friction coefficient between the tape and tensile wire, the transition distance ratio and the tape's shear modulus.

(a) Tensile wire

(b) Steel bar

Figure 3: The tensile wire was cut from the same test pipe in the full scale testing. The steel bar was separately manufactured for achieving full contact.

The components in the cross section may also suffer from high temperature in operation condition. The manufacturing procedure or high temperature and contact pressure in-service conditions may result in creep deformation of the anti-wear tapes, where permanent grooves are formed by the geometry of tensile wires along the longitudinal direction. Therefore, the friction in longitudinal direction and transverse direction may be different, which is the focus of the proposed anisotropic friction model.

3.2. Basic relations

For the contact surface, a coordinate system $(\bar{\boldsymbol{e}}_{\boldsymbol{1}}, \bar{\boldsymbol{e}}_{\boldsymbol{2}}, \bar{\boldsymbol{n}})$ is defined. The base vectors $\bar{\boldsymbol{e}}_{\boldsymbol{1}}$ and $\bar{\boldsymbol{e}}_{\boldsymbol{2}}$ are principal vectors corresponding to the longitudinal and transverse directions, respectively. $\bar{\boldsymbol{n}}$ is the normal vector pointing to the direction to make a right-hand coordinate system. The traction vector is given by:

$$\begin{aligned} \boldsymbol{f} &= \boldsymbol{f_t} + \boldsymbol{f_n} \\ &= f_{t1}\bar{\boldsymbol{e}}_{\boldsymbol{1}} + f_{t2}\bar{\boldsymbol{e}}_{\boldsymbol{2}} + f_n\boldsymbol{n} \end{aligned} \tag{1}$$

where f_{t1} and f_{t2} correspond to the longitudinal, transverse friction forces, respectively, and f_n is the normal contact force.

When there is relative motion between contact surfaces, stick and sliding are two distinguished situations. Before the maximum static friction is exceeded by shear force, the relative movement will be restrained. After that, the helix elements start to slide on the contact surface. The constraints for the sliding condition were summarized in Litewka's work [18] based on the concept of plasticity. According to the approach with analogy to plasticity, the relative displacement $\boldsymbol{u}$ can be divided into an elastic part (superscript e) and a plastic part (superscript p), representing the stick and sliding conditions, respectively.

$$\begin{aligned} \boldsymbol{u} &= \boldsymbol{u_t} + \boldsymbol{u_n} \\ &= (\boldsymbol{u_t^e} + \boldsymbol{u_t^p}) + (\boldsymbol{u_n^e} + \boldsymbol{u_n^p}) \\ &= (u_{t1}^e \bar{\boldsymbol{e}}_{\boldsymbol{1}} + u_{t2}^e \bar{\boldsymbol{e}}_{\boldsymbol{2}}) + (u_{t1}^p \bar{\boldsymbol{e}}_{\boldsymbol{1}} + u_{t2}^p \bar{\boldsymbol{e}}_{\boldsymbol{2}}) + (u_n^e \boldsymbol{u_n} + u_n^p \boldsymbol{u_n}) \end{aligned} \tag{2}$$

The elastic relative displacement is either zero or a small quantity from micro-displacement which corresponds to rigid-ideally plastic and elastic-ideally plastic material models, respectively. In the rigid-ideally plastic model, the constraint of relative tangential displacement is in the following form:

$$\boldsymbol{u^e} = 0 \tag{3}$$

With analogy to the stress and strain relationship, the traction and relative displacement between two surfaces can also be modeled based on plasticity theory. In the penalty method, The traction vector is defined as:

$$\boldsymbol{f} = \boldsymbol{C^e}(\boldsymbol{u} - \boldsymbol{u^p}) \tag{4}$$

where

$$\boldsymbol{C^e} = \alpha_{t1} \bar{\boldsymbol{e}}_{\boldsymbol{1}} \otimes \bar{\boldsymbol{e}}_{\boldsymbol{1}} + \alpha_{t2} \bar{\boldsymbol{e}}_{\boldsymbol{2}} \otimes \bar{\boldsymbol{e}}_{\boldsymbol{2}} + \alpha_n \bar{\boldsymbol{n}} \otimes \bar{\boldsymbol{n}} \tag{5}$$

where α_{t1}, α_{t2} and α_n are the penalty parameters [18]. In the penalty method, the constraint condition can only be satisfied when $\alpha = +\infty$. However, it is well known that the penalty parameter must be selected as a compromise by also considering convergence issues. Therefore, the constraint condition has to be fulfilled within a certain tolerance by selecting the penalty parameter value. This method constitutes an analogy to a more general elastic-ideally plastic material model, where the penalty parameter is the counterparts of the elasticity modulus. For beam contact applications as focused in the present paper, the penalty parameter also plays the role of representing the surface and shear stiffness in the through thickness direction, thus enabling reasonable penalty values to be used without compromising the physical behavior.

In a similar way, the sliding velocity is additively decomposed into elastic and plastic parts :

$$\begin{aligned} \boldsymbol{v} &= \boldsymbol{v_t} + \boldsymbol{v_n} \\ &= (\boldsymbol{v_t^e} + \boldsymbol{v_t^p}) + (\boldsymbol{v_n^e} + \boldsymbol{v_n^p}) \\ &= (v_{t1}^e \bar{\boldsymbol{e}}_{\boldsymbol{1}} + v_{t2}^e \bar{\boldsymbol{e}}_{\boldsymbol{2}}) + (v_{t1}^p \bar{\boldsymbol{e}}_{\boldsymbol{1}} + v_{t2}^p \bar{\boldsymbol{e}}_{\boldsymbol{2}}) + (v_n^e \bar{\boldsymbol{n}} + v_n^p \bar{\boldsymbol{n}}) \end{aligned} \tag{6}$$

The corotational rate of traction is given by:

$$\mathring{\boldsymbol{f}} = \dot{\boldsymbol{f}} - \boldsymbol{\Omega} \boldsymbol{f} \tag{7}$$

where the skew-symmetric tensor $\boldsymbol{\Omega}$ is the spin describing the rigid-body rotation of the contact surface. In the present work, the spin is assumed zero because the co-rotated formulation is used in the FE framework applied here. The co-rotational rate of traction has the relation with velocity based on Eq.4 as follows:

$$\mathring{\boldsymbol{f}} = \boldsymbol{C^e} \boldsymbol{v^e} \tag{8}$$

In the present friction model, the elastic relative displacement is determined by the sliding direction and the yield surface which expands or shrinks depending on the dynamic contact pressure.

3.3. Sliding yield function and sliding potential function

The dry contact friction on a rough contact surface has been based on an analogy to perfect plasticity in the literature [7, 8, 10, 11, 12, 19] where the friction has been assumed to follow the plastic flow after the friction limit was reached. Therefore, the sliding rules of the contact surface can be derived by the velocity rules which either may be associated with the friction limit function, or non-associated by a separate sliding potential function.

An elliptical function representing the anisotropic friction limit was studied by Michalowski and Mroz [7, 10]. The friction sliding yield function $\boldsymbol{F}$ and the sliding potential function $\boldsymbol{G}$ were given by :

$$F(f_{t1}, f_{t2}, f_n) = \left(\left(\frac{f_{t1}}{C_1} \right)^2 + \left(\frac{f_{t2}}{C_2} \right)^2 \right)^{1/2} - \mu f_n = 0 \tag{9}$$

$$G(f_{t1}, f_{t2}, f_n) = \left(\left(\frac{f_{t1}}{B_1} \right)^2 + \left(\frac{f_{t2}}{B_2} \right)^2 \right)^{1/2} - \beta = 0 \tag{10}$$

where the C_1 and B_1, C_2 and B_2 represent the orthogonal principal friction scaling factors, respectively.

It defines:

$$\boldsymbol{F} = \frac{\partial F}{\partial \boldsymbol{f}}, \quad \boldsymbol{G} = \frac{\partial G}{\partial \boldsymbol{f}} \tag{11}$$

The sliding velocity v_{t1}^p and v_{t2}^p are expressed according to Mroz and Stupkiewicz's work [10] as:

$$\boldsymbol{v_t^p} = \dot{\lambda} \frac{\partial G}{\partial \boldsymbol{f}} = \dot{\lambda} \boldsymbol{G} \tag{12}$$

where

$$\dot{\lambda} = \frac{B_1^2}{C_1} ((v_{t1}^p)^2 + (v_{t2}^p)^2)^{1/2} \tag{13}$$

The material-time derivative of Eq.9 is given by:

$$\boldsymbol{F} \cdot \dot{\boldsymbol{f}} = 0 \tag{14}$$

where

$$\boldsymbol{F} = \frac{\partial F}{\partial \boldsymbol{f_{t1}}} \bar{\boldsymbol{e}}_{\boldsymbol{1}} + \frac{\partial F}{\partial \boldsymbol{f_{t2}}} \bar{\boldsymbol{e}}_{\boldsymbol{2}} + \frac{\partial F}{\partial \boldsymbol{f_n}} \bar{\boldsymbol{n}} \tag{15}$$

Since the skew-symmetric tensor $\boldsymbol{\Omega}$ is zero, the corotational rate of traction is equal to the material-time derivative of traction:

$$\dot{\boldsymbol{f}} = \mathring{\boldsymbol{f}} = \boldsymbol{C^e} (\boldsymbol{v} - \boldsymbol{v^p}) \tag{16}$$

Inserting Eq.12,13 into Eq.16, it gives:

$$\boldsymbol{F}^T \boldsymbol{C^e} (\boldsymbol{v} - \dot{\lambda} \boldsymbol{G}) = 0 \tag{17}$$

Then $\dot{\lambda}$ is written as:

$$\dot{\lambda} = \frac{\boldsymbol{F}^T \boldsymbol{C}^e \boldsymbol{v}}{\boldsymbol{F}^T \boldsymbol{C}^e \boldsymbol{G}} \tag{18}$$

By inserting Eq.18 into Eq.16:

$$\mathring{\boldsymbol{f}} = \boldsymbol{C}^e(\boldsymbol{v} - \frac{\boldsymbol{F}^T \boldsymbol{C}^e \boldsymbol{v}}{\boldsymbol{F}^T \boldsymbol{C}^e \boldsymbol{G}} \boldsymbol{G}) = \boldsymbol{C}^e(\boldsymbol{I} - \frac{\boldsymbol{G} \otimes \boldsymbol{F}^T \boldsymbol{C}^e}{\boldsymbol{F}^T \boldsymbol{C}^e \boldsymbol{G}})\boldsymbol{v} = \boldsymbol{C}\boldsymbol{v} \tag{19}$$

where $\boldsymbol{I}$ is the identity matrix and $\boldsymbol{C}$ is the stiffness matrix.

In Belytschko et al. [16], the non-associated potential flow rule was selected to exclude effects from irreversible slip in the normal direction $\boldsymbol{v_n^p} = \dot{\lambda}\partial F/\partial f_n$. However, the stiffness matrix $\boldsymbol{C}$ obtained from the non-associated potential flow rule was unsymmetrical. This causes difficulties with respect to application in the present computer code where a symmetric solver is applied. Therefore, the friction scaling factors in the yield function and potential flow rule were set to $C_1 = B_1$, $C_2 = B_2$ and β to be constant in order to formulate a symmetric stiffness matrix in the tangential plane. In addition, the components related to contact force coupling were set to zero to avoid irreversible slip due to normal displacement and also to ensure a symmetric stiffness matrix $\boldsymbol{C}$. This implies that the stiffness matrix is not exactly obtained from the yield function and flow rule and more iterations might be needed in the calculation.

4. Experimental results and discussions

Three small scale tests (Test No.1 - Test No.3) were carried out for measuring the friction coefficient under variable contact pressure, the transition distance ratio, the shear modulus of the anti-wear tape and studying the friction behavior in groove track.

4.1. Test No.1: Measuring friction coefficients under variable contact pressure

For Test No.1, it was aimed to measure the static and dynamic friction coefficients of the contact interface as it was in the flexible pipe under variable contact pressure corresponding to 8MPa, 4MPa and 1MPa, respectively, by assuming constant frequency 0.01 $[Hz]$. The in-service tape outer surface (Figure 2a) and tensile wire (Figure 3a) were used. Some oil and rust spots were observed on the tape and tensile wire surface. After the tests, about 50% full contact was observed which was related to difficulties in sufficiently straightening the curved wire. The out-of-straightness also caused peak values before the friction reversed as seen in Figure 4a. Larger reverse amplitude was seen under lower contact pressure because less contact area was activated under less contact pressure and less straightness. The static and dynamic friction coefficients were found to be determined by the contact surface properties (contact surface irregularity and contact surface type). The static and dynamic friction coefficients were selected as the maximum (in the stick domain) and minimum values in Figure 4a. The static friction coefficients were measured to be 0.22, 0.24, 0.38 corresponding to the contact pressure 8MPa, 4MPa and 1MPa, respectively. The corresponding dynamic friction coefficients were 0.18, 0.20 and 0.32, see Figure 4a. The contact pressure was 4 $[MPa]$ between the inner wire and anti-wear tape whereas it was 2 $[MPa]$ between the outer wire and anti-wear tape after applying full internal pressure 20 $[MPa]$ and initial strain 0.02 [1]. The effective dynamic friction coefficient was on that basis estimated to be 0.21, which was equal to the value obtained from the full scale test. This suggests that it is possible and accurate to measure the friction coefficient between the tape and tensile wire by small scale testing. This is also confirmed by the observation that both the static and dynamic friction coefficients decreased with increasing contact pressure as observed in the full scale testing.

4.2. Test No.2: Measuring transition distance ratio and shear interaction stick stiffness

For Test No.2, it was aimed to measure the anti-wear tape's shear modulus. The validation tests in Section 2.2 concluded that the shear modulus was affected by the contact surface area. The full contact surface can guarantee the shear modulus measurement accuracy. Therefore, this test applied the clean tape surface

(Figure 2b) and a tailor-made steel bar (Figure 3b). In addition, the tapes were squeezed for 48 hours to form a full contact surface. This test was carried out under constant frequency 0.01 $[Hz]$ and constant contact pressure 4 $[MPa]$.

The tape's shear stress is given as:

$$\tau = G\frac{u}{t} \tag{20}$$

where u is anti-wear tape deformation, t is the tape's thickness 1.8 $[mm]$, G is the tape's shear modulus.

The tangential force considering both tape surfaces is obtained by inserting $F = 2\tau wl$:

$$F = 2G\frac{wl}{t}u \tag{21}$$

where F is the friction force, w is width of steel bar, l is length of the contact area.

Then the slope of friction measurements versus relative displacement is written by:

$$k = 2G\frac{wl}{t} \tag{22}$$

where k is the slope of friction versus relative displacement. The shear interaction stick stiffness applied in the friction model [1] is then defined by:

$$K_0^{t1} = G_{eff}\frac{w}{t} \tag{23}$$

where G_{eff} is the tape's effective shear modulus, w is the tensile wire's width and t is the total thickness of the supporting plastic layers. The analytical solution of K_0^{t1} was proposed in [1]. The effective shear modulus of anti-wear tape was obtained as 274.4 $[MPa]$ based on Eq.23.

A slope equal to 30488 $[N/mm]$ was obtained in the beginning of the stick domain which resulted in a shear modulus of 274 $[MPa]$. It suggests that the measured shear modulus can be used to calculate K_0^{t1}. Relatively constant dynamic friction was achieved when using the steel bar and squeezed tape, see Figure 4b. The increase introduced by out-of-straightness was also eliminated. The average constant dynamic friction was selected as indicated in Figure 4b. The transition displacement was obtained when the shaded areas were identical. The transition distance ratio was obtained equal to 2.0 which was according to the assumed transition distance ratio in [1].

4.3. Test No.3: Investigating friction behavior in groove track

For Test No.3, it was aimed to study the friction behavior when the tensile wire was in the groove track as it was in the flexible riser under variable frequency, e.g. 0.01, 0.05, 0.1, 0.2 $[Hz]$ and constant contact pressure 4 $[MPa]$. Therefore, the in-service tape inner surface (Figure 2c) and tensile wire (Figure 3a) were applied. Since there were irregularities on both tape and tensile wire surfaces, full contact surface could not be achieved. Therefore, the dynamic friction increased after a relatively constant regime when it approached to the reverse point as illustrated in Figure 4c. The static friction coefficient decreased 8% with increased frequency from 0.2 $[Hz]$ to 0.01 $[Hz]$. It occurred because the higher frequency may amplify the misalignments effect due to the irregularities of tensile armor and tape's surface whereas it had less effect on the dynamic friction coefficient.

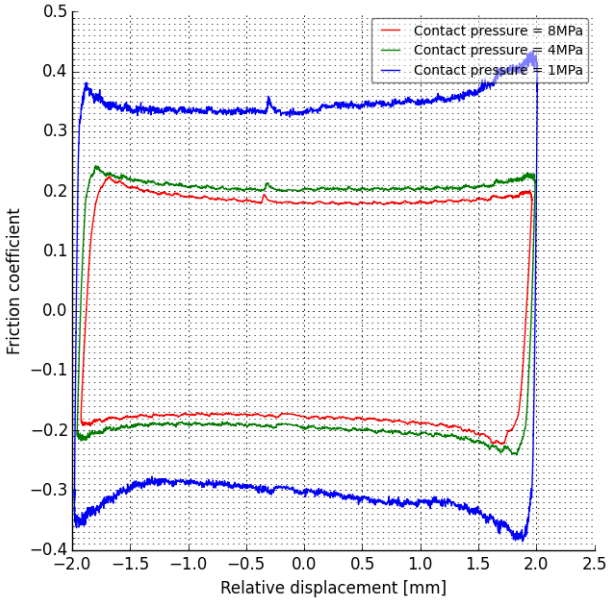

(a) Test No.1

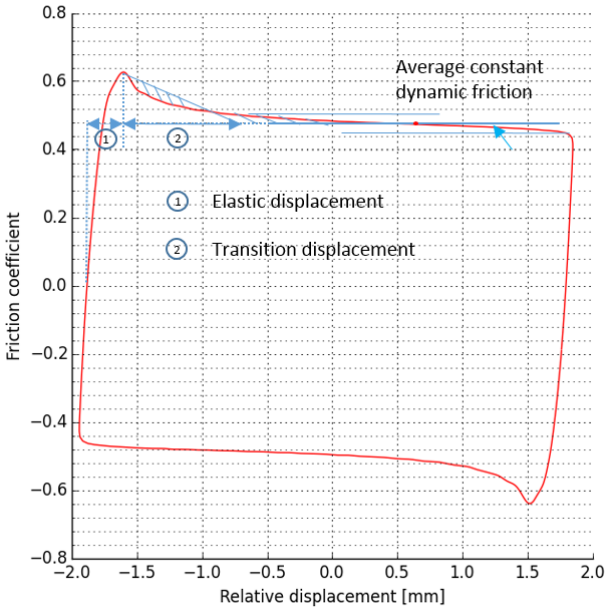

(b) Test No.2

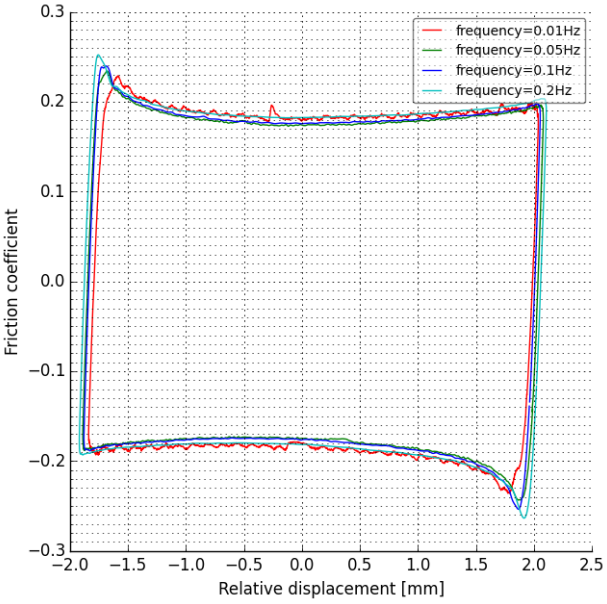

(c) Test No.3

Figure 4: Three small scale tests were carried out for measuring friction coefficients under variable contact pressure, the transition distance, the tape's shear modulus and the friction coefficients under variable frequency.

4.4. Summary

The main findings from small scale testing are summarized as follows:

1. Decreasing friction coefficients were observed under increasing contact pressure.
2. Small scale testing was found able to measure the friction coefficient observed from full scale testing.
3. The anti-wear tape's shear modulus could also be measured as long as full contact was obtained.
4. The transition distance ratio was measured, confirming the assumptions and conclusions in [1].

5. Testing of the anisotropic friction algorithm

5.1. Introduction

The longitudinal and transverse friction forces are determined by the friction scaling factors (C_1, C_2), shear interaction stick stiffness (K_0^{t1}, K_0^{t2}), contact force (f_n), friction coefficient (μ) and sliding angle (γ). Three cases were studied for investigating C_2, K_0^{t2} and γ effects on the friction forces as shown in Table 1. In all cases, the relative displacements in two directions are harmonic. The friction scaling factor and shear interaction stick stiffness were set to $C_1 = C_2 = 1$ and $K_0^{t1} = K_0^{t2} = 300[MPa]$, respectively. The effects of $C_2 = 10$ and $K_0^{t2} = 600[MPa]$ were investigated under sliding angle $\gamma = 26°$ and $3°$, respectively, corresponding to Case 1 and Case 2. The dynamic contact force effect on friction forces was studied in Case 3 where a harmonic variable contact force was assumed under sliding angle $\gamma = 26°$.

Table 1: Three cases were used to investigate the friction scaling factor, shear interaction stick stiffness, contact force and sliding direction effects on the friction forces. The corresponding inputs for each case is shown where u_{t1} and u_{t2} are longitudinal and transverse relative displacements, f_n is contact force, γ is sliding angle.

No.	u_{t1} [mm]	u_{t2} [mm]	C_1	C_2	$K_0^{t1}[MPa]$	$K_0^{t2}[MPa]$	f_n [N/m]	γ
Case 1	0.06sin(2πt)	0.03sin(2πt)	1	1,10	300	300, 600	5000	26°
Case 2	0.06sin(2πt)	0.003sin(2πt)	1	1,10	300	300, 600	5000	3°
Case 3	0.06sin(2πt)	0.03sin(2πt)	1	1	300	300	5000sin(2πt)+10000	26°

The friction forces in two directions are obtained by elastic stiffness matrix and elastic relative displacement u_e as given in Eq.8 in the friction algorithm. The u_e is determined by the yield surface function defined as:

$$\left(\frac{u_{e1}}{\frac{C_1}{K_0^{t1}}}\right)^2 + \left(\frac{u_{e2}}{\frac{C_2}{K_0^{t2}}}\right)^2 = (\mu f_n)^2 \tag{24}$$

where u_{e1} and u_{e2} are elastic relative displacements in two directions. The yield surface function indicates that it expands with increasing C_2 assuming constant $C_1, K_0^{t1}, K_0^{t2}, \mu$ and f_n (see Figure 5a) whereas it shrinks with increasing K_0^{t2} assuming constant C_1, C_2, K_0^{t1}, μ and f_n (see Figure 5b).

5.2. Case 1: C_2 and K_0^{t2} effects on the friction forces under sliding angle 26°

The C_2 and K_0^{t2} effects on the friction forces under sliding angle 26° are illustrated in Figure 6a. The $C_1, K_0^{t1}, K_0^{t2}, \mu$ and f_n were assumed constant when studying the C_2 effect. Since the yield surface expands with increasing C_2 based on this assumption, both u_{e1} and u_{e2} increase. This results in increased friction forces in both directions as illustrated in Figure 6a. Then C_1, C_2, K_0^{t1}, μ and f_n were assumed constant when studying the K_0^{t2} effect. Because the yield surface shrinks based on this assumption, the u_{e1} and u_{e2} decrease with increasing K_0^{t2}. Therefore, the longitudinal friction is seen to decrease due to decreased u_{e1} whereas the transverse friction increases due to twice K_0^{t2}.

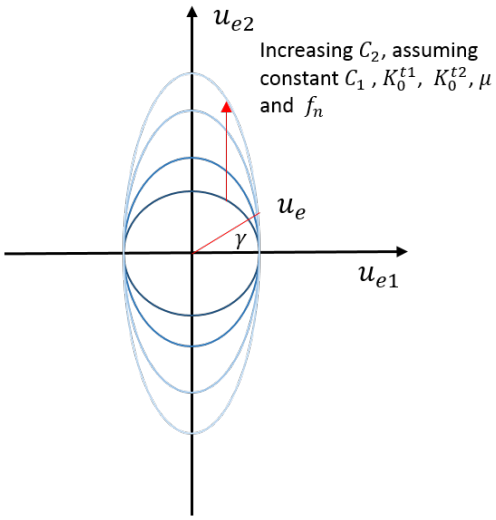

(a) The yield surface expands with increasing C_2, assuming constant C_1, K_0^{t1}, K_0^{t2}, μ and f_n.

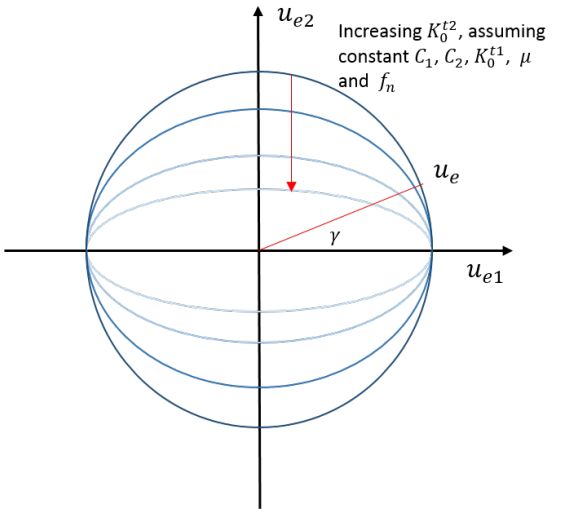

(b) The yield surface expands with increasing K_0^{t2}, assuming constant C_1, C_2,K_0^{t1}, μ and f_n.

Figure 5: The yield surface in terms of elastic relative displacement in longitudinal and transverse directions.

5.3. Case 2: C_2 and K_0^{t2} effects on the friction forces under sliding angle 3°

The C_2 and K_0^{t2} effects on the friction forces under sliding angle 3° are illustrated in Figure 6b. The same study procedures as performed in Case 1 were repeated. It was found that $C_2 = 10$ had small effect on the friction forces. For $K_0^{t2} = 600[MPa]$, this had small effect on the longitudinal friction whereas the transverse friction was twice of the value with $K_0^{t2} = 300[MPa]$. This occurs because the sliding angle is limited to the zone where C_2 and K_0^{t2} have small effect on the u_{e1} and u_{e2}.

5.4. Case 3: dynamic contact force effect on the friction forces

The dynamic contact force effect on the friction forces is demonstrated in Figure 6c. A harmonic contact pressure history was applied with static amplitude 10000 $[N/m]$. If the contact pressure, f_n, is constant equal to 10000 $[N/m]$, the maximum static longitudinal and transverse friction are 1800 and 880 $[N]$, respectively. In the first quarter part in Figure 6c, the f_n increases with increasing displacement. In the stick domain, K_0^{t1} and K_0^{t2} ensure constant stiffness. The maximum static longitudinal and transverse friction were found to be 1869 and 990 $[N]$ as shown in Figure 6c, which are higher than the friction forces with constant f_n, 10000 $[N/m]$. The friction forces continue increasing with increasing f_n after the yield surface is exceeded. This shows that the yield surface expands due to increasing f_n and the anisotropic friction model is able to predict friction forces under dynamic contact pressure with constant shear interaction stick stiffness.

5.5. Summary

Based on the discussions above, the friction scaling factors and shear interaction stick stiffness are able to describe anisotropic friction behavior. They have small effects on the elastic relative displacements in two directions under small sliding angle. In addition, the friction algorithm is found capable of handling friction forces under dynamic contact pressure. Section 7 deals with how the friction algorithm was implemented into the computer code and how it influences the behavior of helical elements.

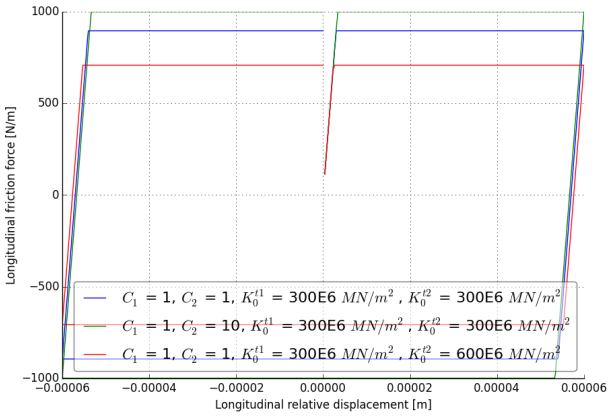

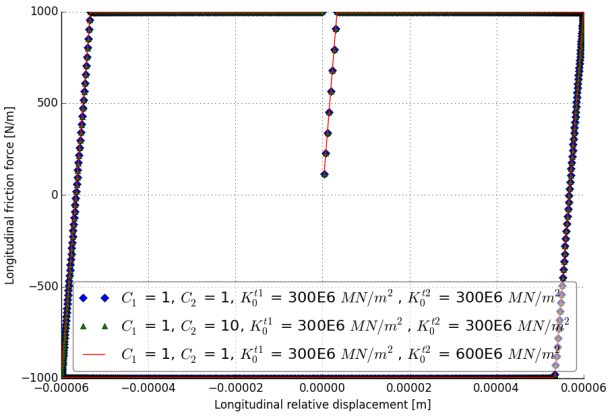

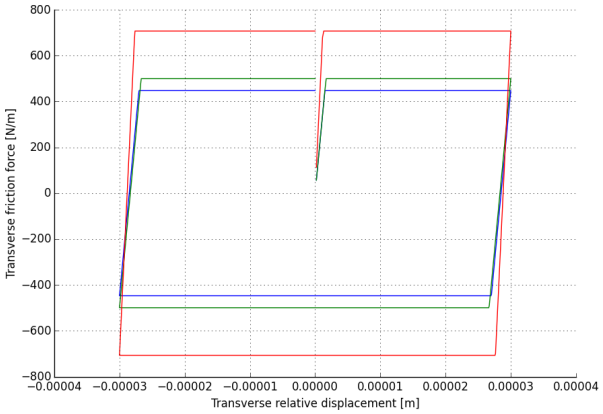

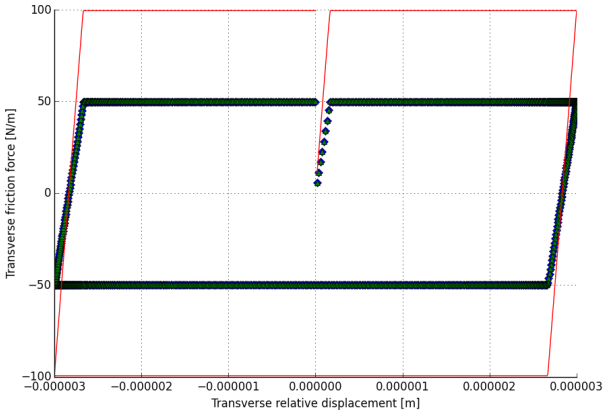

(a) Case 1

(b) Case 2

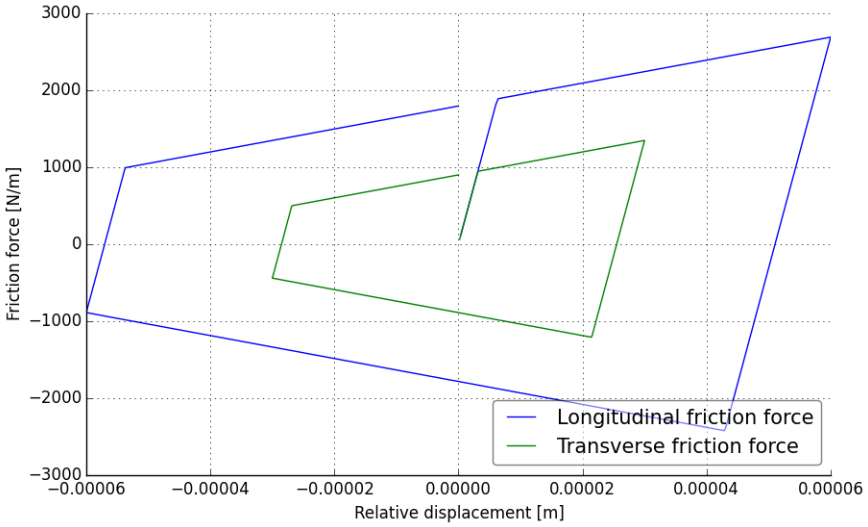

(c) Case 3

Figure 6: The transverse friction scaling factor and shear interaction stick stiffness effects were studied under two sliding angles 26° (Case 1) and 3° (Case 2), respectively. The dynamic contact pressure effect was investigated in Case 3.

6. Finite element implementation and numerical models

6.1. Finite element implementation

The proposed anisotropic friction model was implemented into the HCONT453 and HCONT463 contact elements in BFLEX [20] and applied for numerical studies. HCONT453 is a four node contact element for handling contact between two helix layers, whereas HCONT463 considers contact between a cylindrical layer and one helix layer. They are both based on a hybrid mixed formulation where the contact condition is imposed by means of a penalty surface stiffness parameter [20]. The numerical models presented herein makes use of the structural elements HSHEAR353 and HSHEAR363. HSHEAR363 is a 13 degrees of freedoms (DOFs) element that in addition to the 12 standard beam DOFs includes a radial DOF to describe radial interaction. Two constitutive models are allowed for: one thin shell model for representing the plastic layers and one helix model to represent the axisymmetric forces in the pressure spiral layers. HSHEAR353 is a 24 DOFs curved beam element that in addition to the standard beam DOFs includes 12 local helix DOFs to describe the local displacement relative to the loxodromic path [20, 21, 22]. These elements can be applied for modeling all layers in a flexible pipe. In this section, the friction scaling factor, shear interaction stick stiffness and helical element path effects on the friction forces and axial stress range at outermost fiber position are focused on.

6.2. Simplied numerical model

A simplified numerical model was established. The model consisted of a single tendon with 35° lay angle and 70.3 mm layer radius, and an anti-wear tape layer with radius 67.6 mm and thickness 3 mm. The tendon's cross-section was 5 mm wide and 2 mm thick. The length of the model represented a half pitch of tendon applying 20 elements. The HSHEAR353 curved beam element was used to model the tendon and the HSHEAR363 element was applied to model the supporting structure. The HCONT463 contact element was further used to model the contact between the tendon and the supporting layer with the new 2D anisotropic friction model.

The tendon's left end was fixed and the right end was free. A constant tension of 1000 N was applied at the right end to give contact pressure. Forty cycles curvature between 0.0 and 0.55 $[1/m]$ were applied. The transverse DOFs were set free to allow for the anisotropic friction model. Therefore, the tendon elements were designated to slide and simulate the relative displacement induced by the prescribed cyclic curvature history.

6.3. Full scale numerical model

The same full scale test model was used as it was described in Dai et al.'s work [1] for verifying the 2D friction model. The model included the activated length of 1.35m only. The tensile armor's lay angle was $\pm 38°$ and the pitch length was approximately 0.57m. The pipe cross-section consisted of two cross wound tensile armor layers, four plastic sheath layers including the outer sheath, two anti-wear layers and one pressure barrier. For both the inner and outer tensile armor layer, HSHEAR353 was employed to model the tensile armors with a resolution of 16 wires in the circumferential direction. HSHEAR363 was used for the plastic layers and pressure spiral layer. The contact interface between two tensile armor layers were handled by HCONT453 or HCONT463 and both of them were tested with respect to the full scale test data.

7. Numerical results and discussions

7.1. Investigation of transverse friction scaling factor

This section was aimed to study the transverse friction scaling factor C_2 effect on the friction forces which may influence the transverse displacement and axial stress range at outermost fiber position. The simplified model described in Section 6.2 was applied. The transverse friction scaling factors were set to 1, 2, 3, 4, 5 and 10, respectively, corresponding to transverse friction coefficients of 0.2, 0.4, 0.6, 0.8, 1.0 and 2.0. The K_0^{t1} and K_0^{t2} were set to 150 $[MPa]$. For each load step, the model was converged within 3 iterations for the

isotropic friction model whereas approximately 10 iterations were needed for the anisotropic friction model.

Figure 7 demonstrates the longitudinal and transverse friction forces and contact force at neutral axis. The longitudinal friction was plotted for one cycle in the stable condition. In order to study the C_2 and sliding direction effects on friction forces, Figure 8 illustrates the friction and contact forces together with sliding direction under variable C_2 for half a cycle. Figure 8a shows that the wire gradually slides from u_{e1} towards the u_{e2} axis with increasing sliding angle. This results in smaller u_{e1} and larger u_{e2}, such that the longitudinal friction decreases and transverse friction increases, as shown in Figure 8b and 8c. Then the contact force is seen to decrease when the longitudinal reverses, i.e., the yield surface starting unloading, see Figure 8d. It is thus seen that the transverse friction decreases with yield surface shrinking. Because the wire gradually slides towards the u_{e2} axis, the friction forces are not significantly influenced by the variable C_2. Only 1.7% and 2% increase were found for the average longitudinal and transverse friction ranges when increasing C_2 from 1 to 10.

The friction forces may influence the transverse static and dynamic displacement. The transverse displacement of the contact element at neutral axis was used as an example, see Figure 9a. The axial force Q_1 from global curvature in the wire before slip is given by $Q_1 = -EAcos^2\alpha Rcos\psi\beta_2$ in [5], where EA is the axial stiffness of tensile wire, R is the mean radius of tensile armor layer, α is the tensile armor lay angle, ψ is the angular coordinate starting from the lower side of the pipe and β_2 is the global curvature. The associated shear force q_1 per unit length along the wire needed to maintain the plane surface remain plane condition is obtained by differentiating Q_1 with respect to the length coordinate X^1 and applying the relation $\psi = \frac{sin\alpha}{R}X^1$. The shear force q_1 is obtained as $q_1 = EAcos^2\alpha sin\alpha sin\psi\beta_2$ in [5]. For the transverse direction, the shear force that needs to be mobilized in order to restrain the lateral transverse motion is $q_2 = T\beta_2 sin\alpha$ where T is the mean tension of the wire. It can be seen that the longitudinal driving force is much larger than the transverse one. Therefore, the transverse friction force that needs to be mobilized is also smaller than the longitudinal one, thus resulting in smaller transverse relative displacement. The transverse slip u_2 towards the geodesic path without considering friction and bending stiffness is given according to [6]:

$$u_2 = \frac{R^2}{tan\alpha}\big[\frac{cos^2\alpha}{sin\alpha} + 2sin\alpha\big]sin\psi\beta_2 \tag{25}$$

The transverse slip calculated corresponding to the mean state ($\beta_2 = \frac{1}{2}\times 0.55\ m^{-1}$) is found to be 3.92 $[mm]$ from Eq.25, which represents an upper bound estimate of the transverse position the wire will obtain if a sufficient number of cycles are applied, see Figure 9a. The deviation between the static transverse displacement and the analytical value from Eq.25 is due to the tensile armors' bending stiffness. The transverse friction has no effect on the static transverse displacement since it is determined by the global curvature, mean radius and lay angle as indicated in Eq.25. In addition, the dynamic transverse displacement is also identical regardless of variable C_2 because the transverse friction is not significantly influenced by the variable C_2 as discussed above.

The axial stress range may be influenced by the longitudinal friction of each contact element along a wire from the tensile side to the compressive side. Figure 9b shows the axial stress history at the outermost fiber position. It can be seen that the axial stress range is almost identical regardless of the variable C_2. It occurs because only a 1.7% increase was found with respect to the average longitudinal friction range reduction when increasing C_2 from 1 to 10 as discussed above.

It concludes that the transverse friction scaling factor has small effect on the friction forces resulting in small effect on the axial stress range at the outermost fiber position for the present case.

7.2. Investigation of transverse shear interaction stick stiffness

In addition to the friction scaling factor, the groove geometry effect on the friction forces is also characterized by the shear interaction stick stiffness. The simplified numerical model was applied. This section was aimed

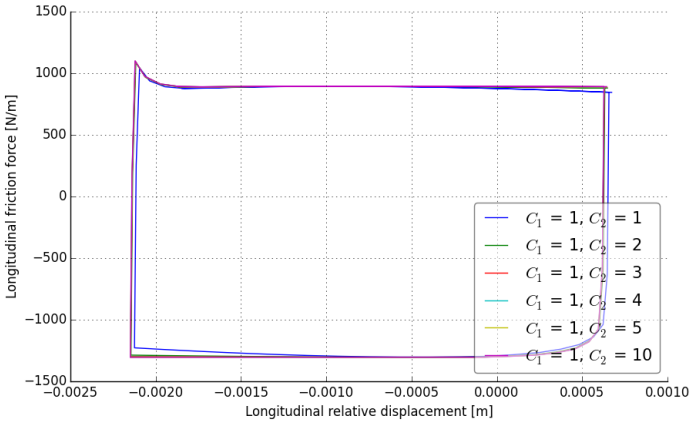

(a) Longitudinal friction force at neutral axis

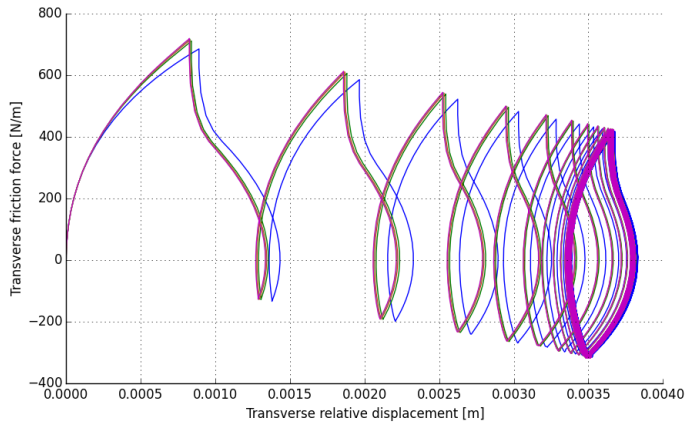

(b) Transverse friction force at neutral axis

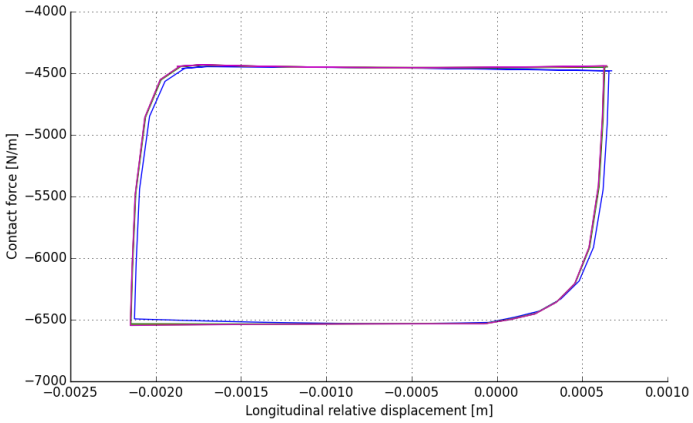

(c) Contact force at neutral axis

Figure 7: Friction behavior at neutral axis under variable transverse friction scaling factor C_2

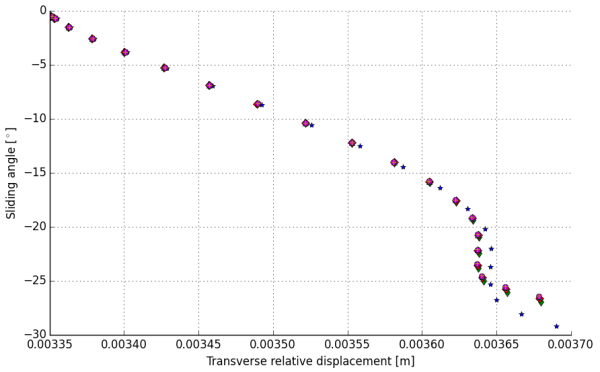

(a) Sliding angle

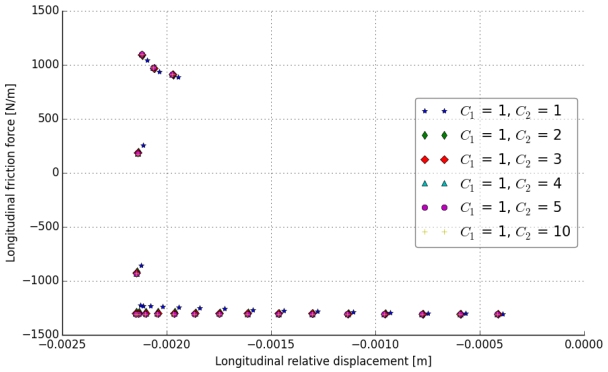

(b) Longitudinal friction force

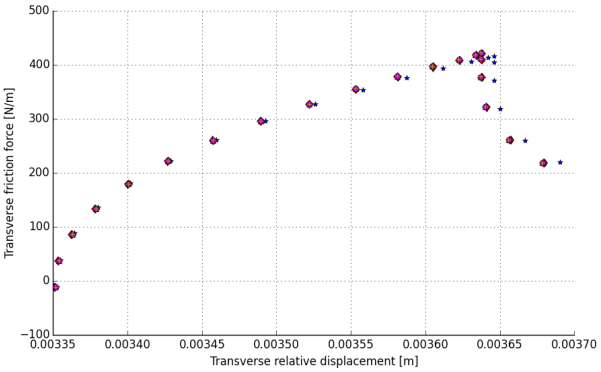

(c) Transverse friction force

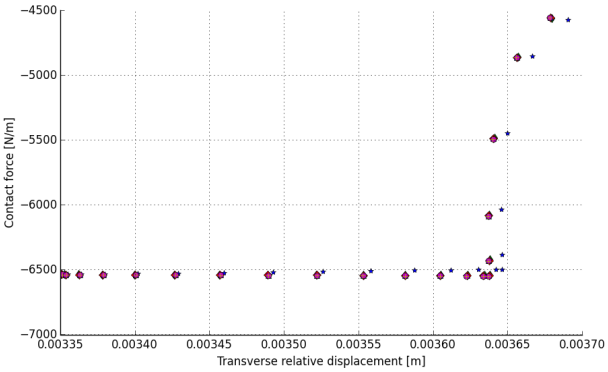

(d) Contact force

Figure 8: Sliding angle, friction forces and contact force of the contact element at neutral axis for half a cycle under variable transverse friction scaling factor C_2.

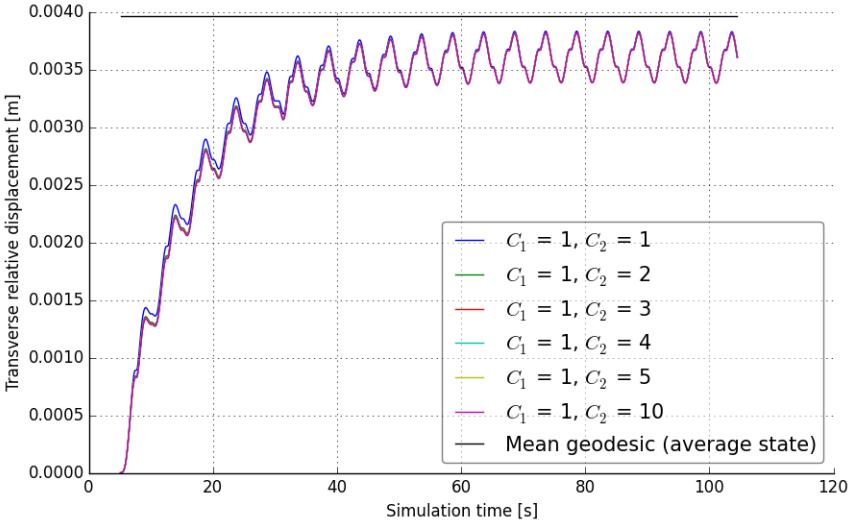

(a) Transverse relative displacement at neutral axis

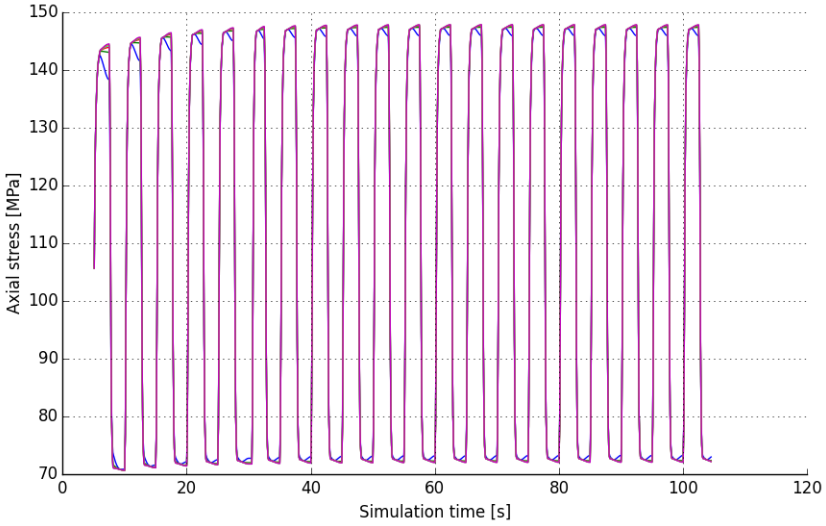

(b) Axial stress of tensile wire at outermost fiber position

Figure 9: Transverse displacement at neutral axis and axial stress range at outermost fiber position under variable transverse friction scaling factor C_2.

to study the K_0^{t2} effect on friction forces and axial stress range at outermost fiber position. The friction scaling factor was set to $C_1 = C_2 = 1.0$. K_0^{t1} was constant with 150 $[MPa]$ whereas K_0^{t2} was set to 150, 200, 300 $[MPa]$, respectively.

Figure 10 shows the longitudinal and transverse friction and contact forces at neutral axis under variable K_0^{t2}. Figure 11 illustrates the sliding angle, longitudinal and transverse friction forces as well as the contact force for half a cycle aiming to study the sliding angle and variable K_0^{t2} effects on the friction forces. Since the contact element with larger K_0^{t2} slides faster towards the u_{e2} axis shown in Figure 11a, the transverse friction with larger K_0^{t2} is also faster approaching to the peak value, see Figure 11c. The transverse friction peak value increases with increased K_0^{t2} because the maximum sliding angle increases with increased K_0^{t2}, see Figure 11c. Only 0.4% increase was found for the average longitudinal friction range when increasing K_0^{t2} from 150 $[MPa]$ to 300 $[MPa]$. However, the average value was found to be 16.3% larger in the transverse direction. It suggests that the transverse shear interaction stick stiffness influences the anisotropic characteristic more significantly than the transverse friction scaling factor in this case.

The transverse friction force may influence the transverse dynamic displacement at neutral axis and axial stress range at outermost fiber position. The transverse displacement under variable K_0^{t2} is shown in Figure 12a. Since a 7% increase for the transverse friction at neutral axis between $K_0^{t2} = 150[MPa]$ and $K_0^{t2} = 300[MPa]$, the dynamic displacement then decreases. The axial stress range is not significantly influenced by the variable K_0^{t2}, see Figure 12b. This is because the 100% increase of K_0^{t2} only induces 0.4% increase for the average longitudinal friction range. It suggests that the axial stress range at outermost fiber position is not significantly influenced by the variable K_0^{t2}. The reason is simply explained that the axial force driving the slip motion is significantly larger than the corresponding transverse force.

7.3. Investigation of helical element path

Since helical elements exposed to bending loads may slip between the limiting paths of the loxodromic and geodesic curves, it is of interest to study the transverse motion effect on the stress range at the outermost fiber position. In this study, both simplified and full scale test models were applied. The geodesic path study applied the isotropic friction model with $C_1 = C_2 = 1.0$, $K_0^{t1} = K_0^{t2} = 150$ $[MPa]$.

By using the simplified model, the longitudinal friction range was found to be only 2% reduced by the transverse motion. Figure 14 shows the average sliding direction (described by $\frac{f_{t1}}{\sqrt{(f_{t1}^2+f_{t2}^2)}}$) in the last cycle. It can be seen that the longitudinal friction accounts for more than 95% of the resultant friction in one cycle. This suggests that the transverse motion is small and the friction force is dominated by the longitudinal effects. Therefore, the axial stress range at outermost fiber position is not significantly influenced as indicated in Figure 13.

In the full scale model, two alternative ways can be applied to simulate the contact interface between two tensile armor layers:

1. By application of HCONT453 where two tensile armor layers are assumed to be interacting directly, by means of the relative displacement between the inner and outer layers which being applied in one friction model. Physically this means that the thin anti-wear tape cannot resist the shear forces but is communicating these directly between the steel wires.

2. By application of HCONT463 where separate friction models are used to represent the interface between the inner wire and the anti-wear tape and the interface between the outer wire and the anti-wire tape.

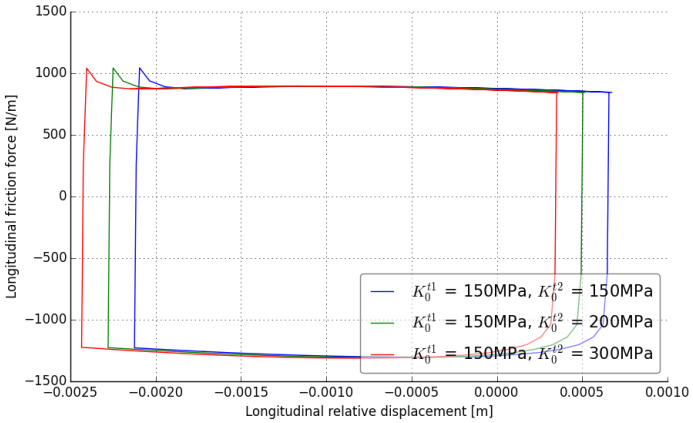

(a) Longitudinal friction force at neutral axis

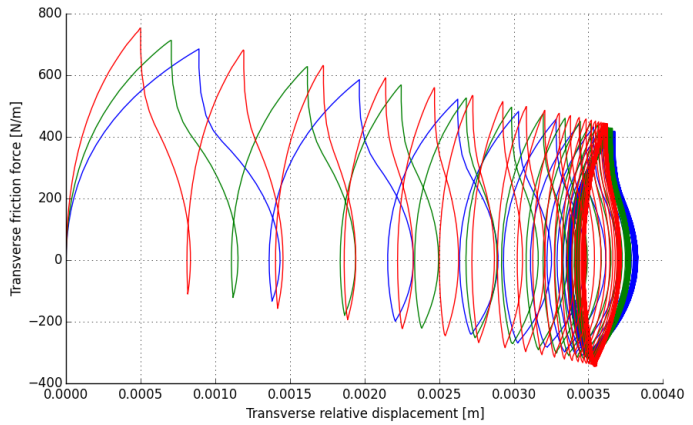

(b) Transverse friction force at neutral axis

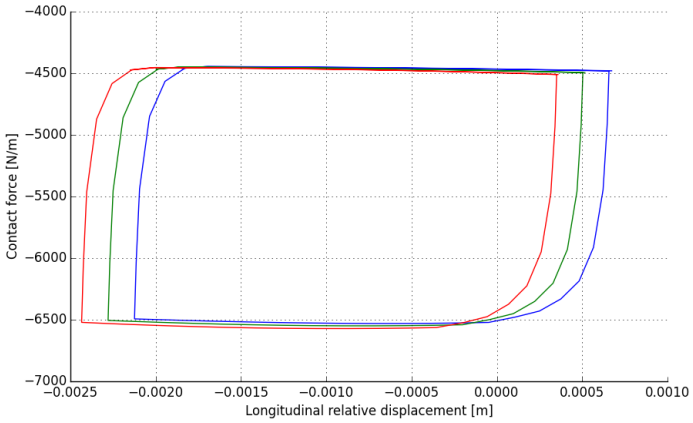

(c) Contact force at neutral axis

Figure 10: Friction behavior at neutral axis under variable transverse shear interaction stick stiffness K_0^{t2}

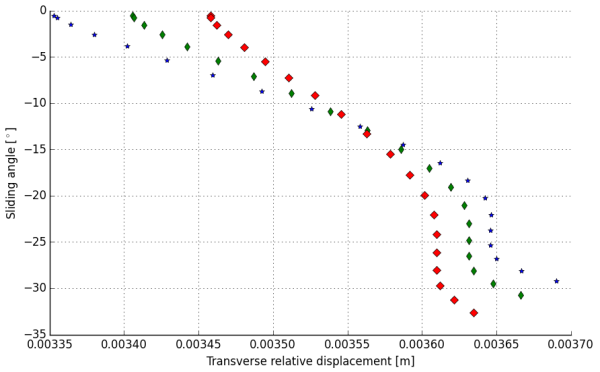

(a) Sliding angle

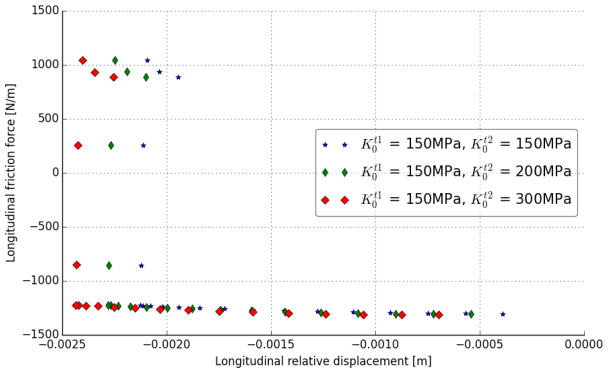

(b) Longitudinal friction force

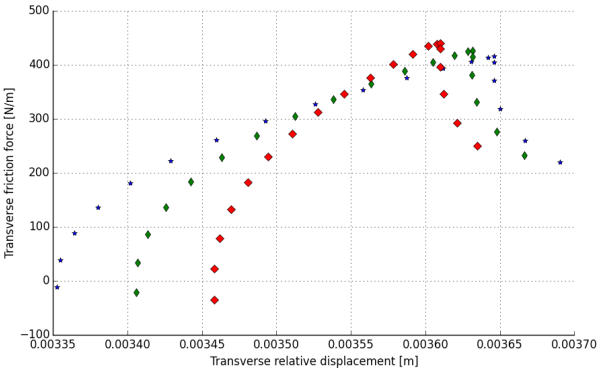

(c) Transverse friction force

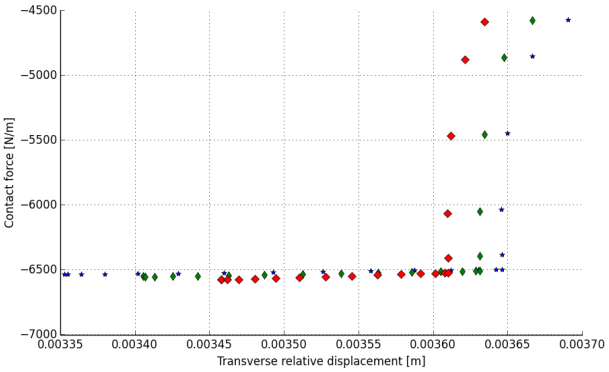

(d) Contact force

Figure 11: Sliding angle, friction forces and contact force of the contact element at neutral axis for half a cycle under variable transverse shear interaction stick stiffness K_0^{t2}

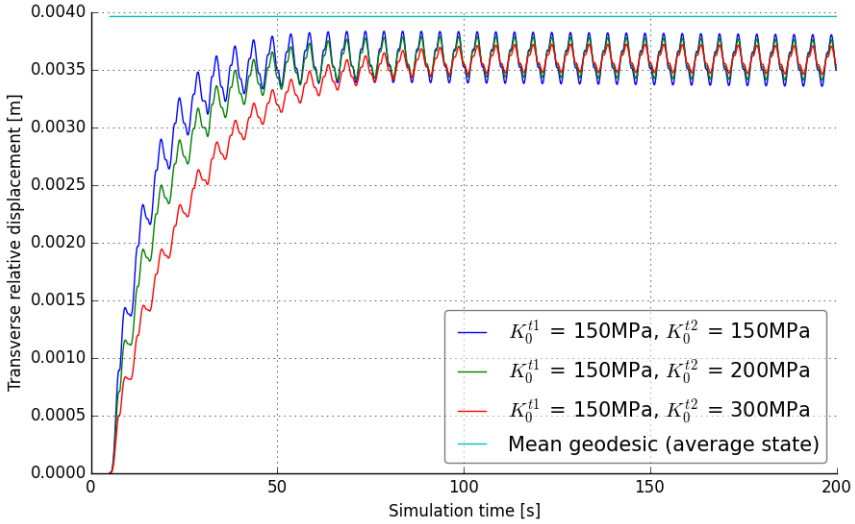

(a) Transverse relative displacement at neutral axis

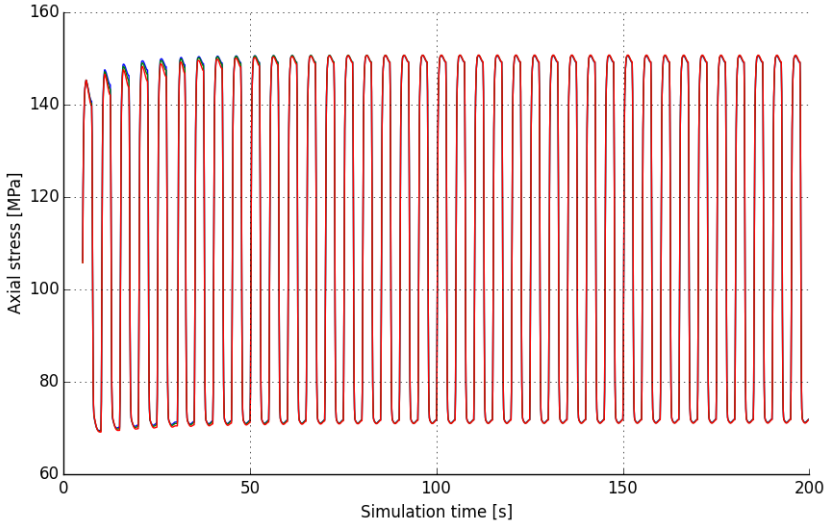

(b) Axial stress of tensile wire at outermost fiber position

Figure 12: Transverse displacement at neutral axis and axial stress range at outermost fiber position under variable transverse shear interaction stick stiffness K_0^{t2}

Both alternative ways were applied in the full scale model in order to investigate how to handle the interface between the tensile wire and anti-wear tape. Firstly, the friction moment obtained by using HCONT463 was found to be 20% higher than by using HCONT463 with 1D friction model, see Figure 16. For HCONT453, if the relative displacement vector is along the pipe's X-axis, the longitudinal friction of the inner and outer armor will be decomposed by the lay angle as $\mu f_n \cos\alpha$ whereas for HCONT463, the same component will be μf_n, thus explaining the 20% difference. Since HCONT453 with measured dynamic friction coefficient from small scale testing showed good correlation with full scale test data, HCONT453 assumption is deemed to be more realistic.

Secondly, the 2D friction model was verified by the full scale testing. It was observed that the axial motion of the outer wire was larger than that of the inner wire, shifting the slip vector towards the outer wire. This results in more friction force is fed into the outer wire. Therefore, the axial stress range of the outer wire by using the 2D friction model increases 67% compared to that by using the 1D friction model whereas a 20% decrease is obtained for the axial stress range of inner wire, see Figure 15. However, the increased axial stress range of the outer wire is compensated by the same amount of decrease in the inner wire. Therefore, the friction moment is not influenced by the 2D model, see Figure 16. It is thus concluded that the axial stress of outer and inner wire may be primarily influenced by the axial motion for multiple helix layers.

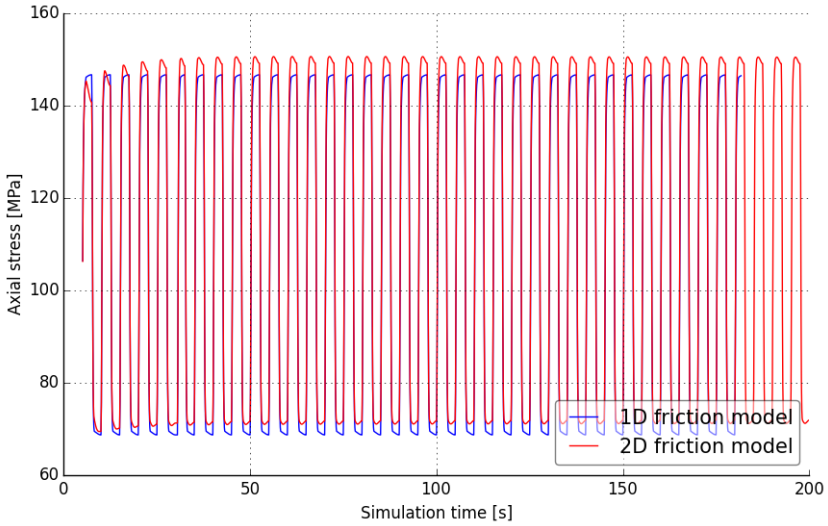

Figure 13: The Loxodromic and geodesic paths effect on the axial stress range at outermost fiber position in the simplified numerical model

7.4. Investigation of transition distance ratio effect

As reported in Test No.2, the transition distance ratio 2.0 was obtained. The transition distance ratio equal to 2.0 was applied in the static friction model in [1] and other ratios were further studied as shown in Figure 17. For the applied friction model, the static and dynamic friction coefficients were equal to respective 0.3 and 0.21 in each case. The comparison results show that the shorter transition displacement gives less effect of static friction on the friction moment. This also validates the current practice of applying a Coulomb friction model with average between static and dynamic friction coefficients will be conservative.

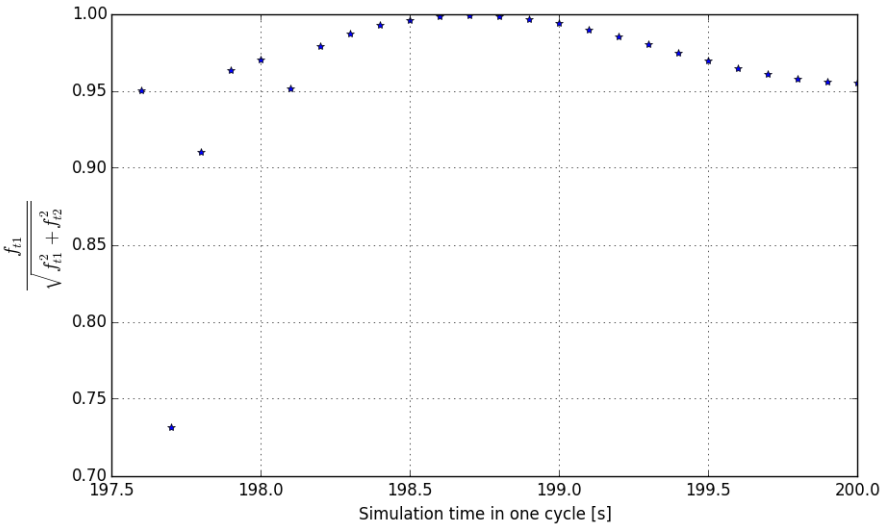

Figure 14: The average sliding direction described by $\frac{f_{t1}}{\sqrt{(f_{t1}^2+f_{t2}^2)}}$ in one cycle of the simplified numerical model

8. Conclusions and future work

- As the decreasing friction coefficients under increasing contact pressure was observed from the full scale test [1], the friction coefficients under dynamic contact pressure were measured by small scale testing. The results were found to correlate very well with the observations from the full scale testing. Similar consistency was also found for the transition distance ratio between static and dynamic friction. For the measured transition distance ratio, the static friction effect was found to be small, implying that the average friction coefficient normally used by industry gives results of sufficient accuracy.

- Due to creep or manufacturing effects, permanent grooves may be formed along the helix path. As it gave extra transverse friction, an anisotropic friction model was proposed aiming to accurately predict the friction forces. Sensitivity studies with respect to the transverse friction scaling factor and shear interaction stick stiffness were carried out by applying a simplified finite element model. It was found that the transverse friction scaling factor and shear interaction stick stiffness did not significantly influence axial stress range at the outermost fiber position.

- HCONT453 element was found more realistic to simulate the contact interface between two layers of tensile armors. Physically this means that the thin anti-wear tape cannot resist the shear forces and the interaction in terms of friction forces between tensile armors is governed by the relative displacements between the two layers.

- The proposed 2D friction model was also verified by full scale testing. It was found that the axial relative motion between layers may cause redistribution of axial stresses between the layers whereas the global moment behavior maintains the same.

- For future work, it is recommended to carry out small scale testing to obtain more data with respect to the transverse shear interaction stiffness and friction coefficients for more tape materials. Since the validation procedure and the model characteristics were only verified by one full scale test in the present work, these should also be verified against other full scale test data.

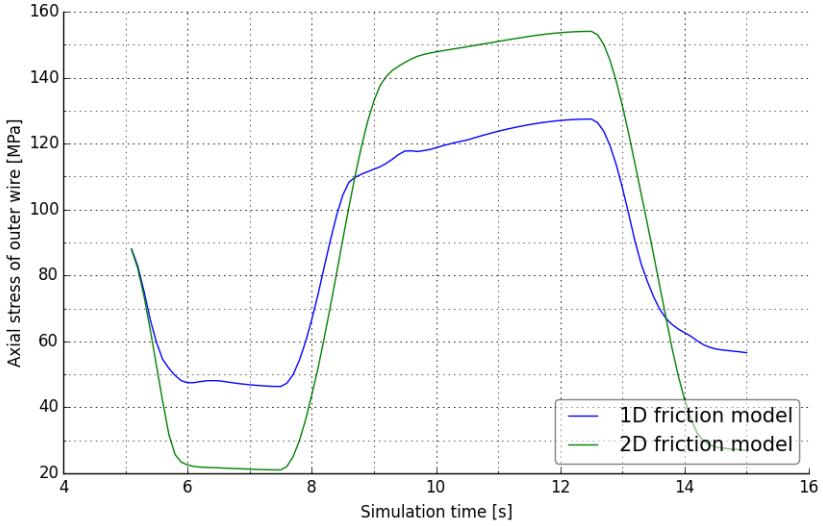

(a) Axial stress of outer wire at outermost fiber position

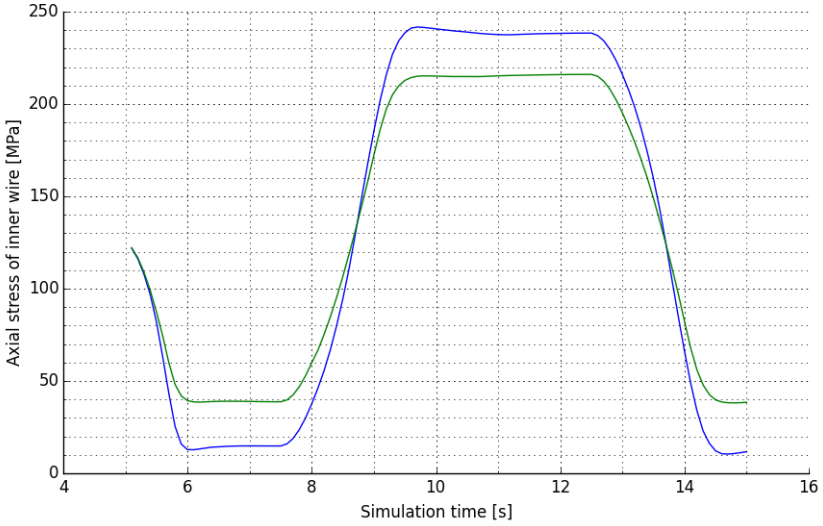

(b) Axial stress of inner wire at outermost fiber position

Figure 15: The Loxodromic and geodesic paths effect on the axial stress range of the outer and inner wires at outermost fiber position in the full scale numerical model

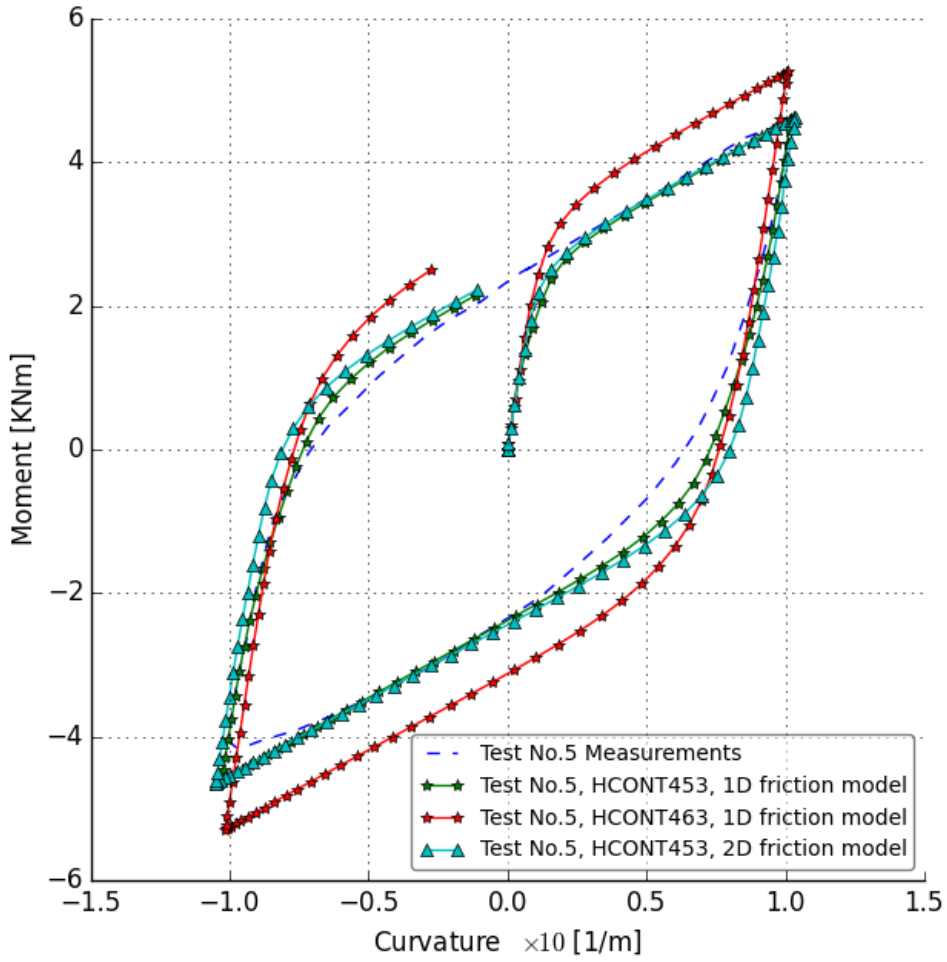

Figure 16: Two contact elements (HCONT453 and HCONT463) were used to model the contact interface between two layers of tensile wires for validating the 2D friction model by the full scale testing.

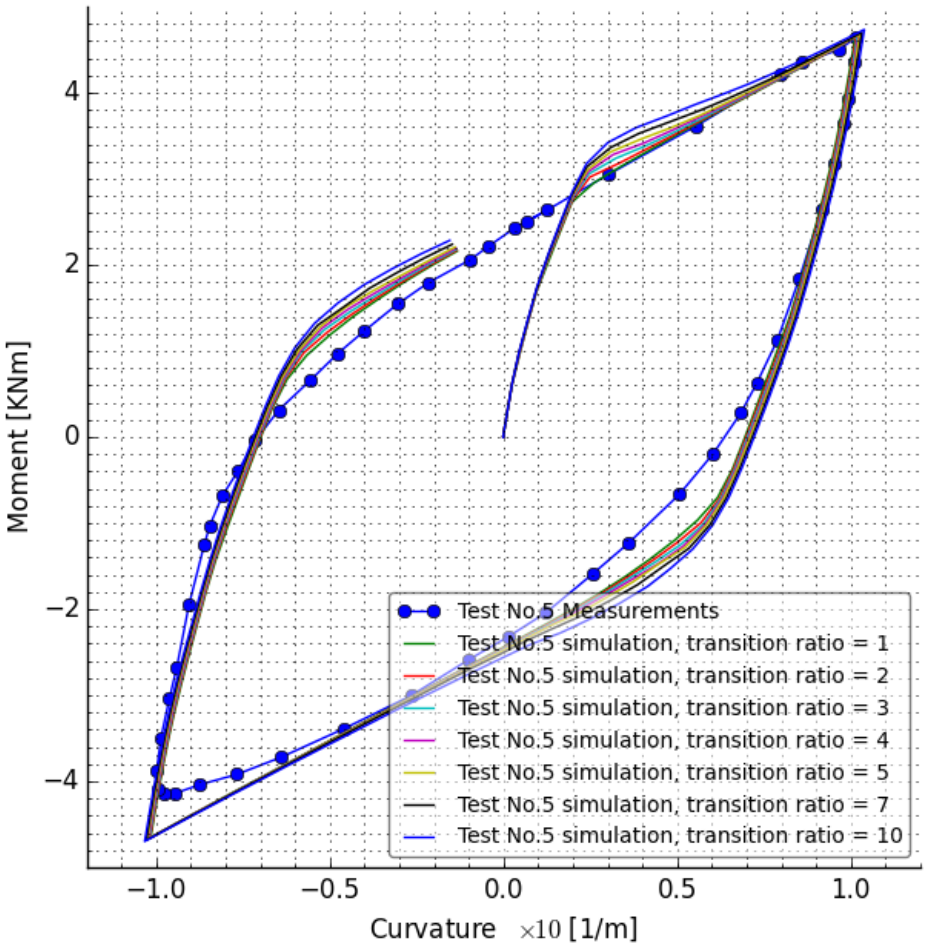

Figure 17: The measured transition distance ratio effects on the friction moment was studied by the full scale testing.

Acknowledgments

The authors would like to appreciate Knut Skjerve, Kristian Aamot, Kristian Minde and Emil Bratlie at SINTEF Ocean for their help in the small scale friction tests. We also appreciate Philippe Maincon for constructive discussions regarding 2D friction model.

Reference

[1] Tianjiao Dai, Svein Sævik, and Naiquan Ye. Friction models for evaluating dynamic stresses in non-bonded flexible risers. *Marine Structures*, 55:137–161, 2017.
[2] B Skallerud. Structrual damping in wellstream pipe. In *Marintek*, 1991.
[3] Svein Sævik and Henan Li. Shear interaction and transverse buckling of tensile armours in flexible pipes. In *ASME 2013 32nd International Conference on Ocean, Offshore and Arctic Engineering*, pages V04AT04A013–V04AT04A013. American Society of Mechanical Engineers, 2013.
[4] Sødahl N, Skeie G, Steinkjer O, and Kalleklev A. Efficient fatigue analysis of helix elements in umbilicals and flexible risers. In *ASME 2010 29th International Conference on Ocean, Offshore and Arctic Engineering*, pages 1029–1037. American Society of Mechanical Engineers, 2010.
[5] Svein Sævik. Theoretical and experimental studies of stresses in flexible pipes. *Computers & Structures*, 89(23):2273–2291, 2011.
[6] Svein Sævik. On stresses and fatigue in flexible pipes. In *Ph.D Thesis*. Norwegian Institute of Technology, Trondheim, Norway, 1992.
[7] R Michalowski. Associated and non-associated sliding rules in contact friction problems. *Archiv. Mech.*, 30:259–276, 1978.
[8] Mohammed Hjiaj, Z-Q Feng, Géry De Saxcè, and Zenon Mróz. On the modelling of complex anisotropic frictional contact laws. *International journal of engineering science*, 42(10):1013–1034, 2004.
[9] A Curnier. A theory of friction. *International Journal of Solids and Structures*, 20(7):637–647, 1984.
[10] Z Mróz and S Stupkiewicz. An anisotropic friction and wear model. *International journal of solids and structures*, 31(8):1113–1131, 1994.
[11] Alfred Zmitrowicz. A theoretical model of anisotropic dry friction. *Wear*, 73(1):9–39, 1981.
[12] Alfred Zmitrowicz. Mathematical descriptions of anisotropic friction. *International journal of solids and structures*, 25(8):837–862, 1989.
[13] K. Hashiguchi and S. Ozaki. Constitutive equation for friction with rotational and orthotropic anisotropy. *Journal of applied mechanics*, 10:383–389, 2007.
[14] K. Hashiguchi and S. Ozaki. Anisotropic constitutive equation for friction with transition from static to kinetic friction and vice versa. *Journal of applied mechanics*, 11:271–282, 2008.
[15] Shingo Ozaki, K Hikida, and K Hashiguchi. Elastoplastic formulation for friction with orthotropic anisotropy and rotational hardening. *International Journal of Solids and Structures*, 49(3):648–657, 2012.
[16] Ted Belytschko, Wing Kam Liu, Brian Moran, and Khalil Elkhodary. *Nonlinear finite elements for continua and structures*. John wiley & sons, 2013.
[17] H Lange, S Berge, Rogne T, and T Glomsaker. Sintef material and chemistry. *Report*, 2004.
[18] Przemyslaw Litewka. *Finite element analysis of beam-to-beam contact*, volume 53. Springer Science & Business Media, 2010.
[19] Alfred Zmitrowicz. Models of kinematics dependent anisotropic and heterogeneous friction. *International Journal of Solids and Structures*, 43(14):4407–4451, 2006.
[20] Svein Sævik. Bflex theory manual. Marintek, 2010.
[21] Svein Sævik. A finite element model for predicting stresses and slip in flexible pipe armouring tendons. *Computers & Structures*, 46(2):219 – 230, 1993.
[22] TY Chang, AF Saleeb, and SC Shyu. Finite element solutions of two-dimensional contact problems based on a consistent mixed formulation. *Computers & structures*, 27(4):455–466, 1987.
[23] Svein Sævik and Naiquan Ye. *Aspects of design and analysis of offshore pipelines and flexibles*. Southwest Jiaotong University Press, 2016.